Resonance Effects from Substituents on L-Type Ligands Mediate Synthetic Control of Gold Nanocluster Frontier Orbital Energies

Hanna Morales Hernández,[†] Satoshi Ohtsuka,[†,‡] Arshad Mehmood,[†,‡] Jake Bordenca,[†] Wangshu Wen,[†] Benjamin G. Levine,[†,‡] and Christopher J. Johnson[*,†]

[†]*Department of Chemistry, Stony Brook University, Stony Brook, NY 11794*

[‡]*Institute for Advanced Computational Science, Stony Brook University, Stony Brook, NY 11794*

E-mail: chris.johnson@stonybrook.edu

Phone: (631) 632-7577

Abstract

The ligands of metal nanoclusters exert a profound effect on their properties and reactivity, but a systematic explanation for these impacts comparable to that of mononuclear coordination complexes does not currently exist. We show that *para*- substituted ligands in prototypical Au-PPh_3 nanoclusters drive changes to frontier orbital energies through resonance effects that span the exterior of the ligand shell to the HOMO and LUMO orbitals centered in the cluster core. Hammett studies of PPh_3 ligands with *para*- and *meta*- methyl and methoxy groups indicate that electronic resonance effects dominate electrostatic effects in controlling the optical HOMO-LUMO gap, but do not specify whether resonance effects simply modulate the charge of the P atom

or extend into the cluster core. Quantum chemical calculations show no significant trend in charge on the Au atoms with respect to electron donating strength of the ligand substituent, but do show a pattern of alternating shortened and lengthened bonds that includes the Au-P bond, suggesting that putative resonance structures include Au atoms. Computed orbitals show a substantial contribution from the atomic orbitals of the ligand substituent to the HOMO orbital only for the *para-* case, mediated by phenyl ring and phosphorous orbitals. These results suggest that a resonance picture must exist that includes the superatomic orbitals of the nanoclusters and, potentially, nanoparticles, even in the ground state. These resonance effects can be used to engineer cluster properties and reactivity predictably *via* simple ligand derivatization and to modulate energy and charge transfer in and out of nanoclusters.

Introduction

Atomically-precise nanoclusters promise many of the desirable features of both nanoparticles and molecules. They typically have large absorption coefficients from the near infrared to the ultraviolet,[1] a large but finite electronic density of states,[2] small redox potentials,[3] and tunability through changes in size, structure, doping, and ligands.[4] At the same time, it is sometimes possible to purify them with exact compositional specificity, and thus exact synthetic control of their properties and behaviors is concievable using traditional chemical approaches. Their amenability to purification also allows their structures to be determined exactly using crystallography, revealing nanoscale structure-function relationships.[5] This has led to a wide range of studies proposing nanoclusters as "designer" nanoparticles in contexts varying from biological sensing to catalysis.

The tunability of nanocluster size, structure, and composition yields three approaches to optimizing their properties in discrete steps for a given task. The smallest step in size is a difference of a single atom, but more typically, specific numbers of atoms are geometrically and electronically stable,[6,7] and thus it is difficult to isolate clusters resulting from the

stepwise addition or exchange of single atoms.[8] Similarly, for a given number of atoms, only one or a few structures are typically known.[9] Tuning by doping[10] or by ligand exchange[11] can allow the fine-grained tuning of nanocluster properties, but can also make the purification of the resulting synthetic mixture much more challenging.[12]

Fine-tuning of molecules and coordination complexes is often achieved by chemical derivatization.As a result, well-developed frameworks exist for predicting how ligand derivatives affect electronic structure and properties of molecules and coordination complexes via bonding,[13] electron withdrawing and donating effects,[14] and steric effects,[15] for example. Such a framework does not yet exist for nanoclusters, hampering the ability to rationally harness ligand chemistry to optimize nanocluster properties.

Nanoclusters formed from gold and phosphine ligands were among the first gold nanoclusters to be isolated and characterized crystallographically.[16] In contrast to X-type thiolate ligands, L-type phosphine ligands can be expected to strongly electronicially couple to the cluster core and thus to exert more influence over the electronic properties of the cluster. For instance, substitution of a single PPh_3 ligand by an N-heterocyclic carbene ligand has been shown to significantly enhance the galvanic efficiency of catalytic Au_{11} clusters.[17] Mingos reported the crystal structures and spectra of a series of derivatives of $Au_9(PPh_3)_8^{3+}$ featuring -Me or -OMe substituents in the *para*- positions of the PPh_3 ligands which showed that substitution induced marked changes in the electronic spectra of the clusters, but these changes were masked by gross structural rearrangement induced by the ligands in the solid state.[16,18] The $Au_9(PPh_3)_8^{3+}$ and closely-related $Au_8(PPh_3)_7^{2+}$ nanoclusters have been extensively investigated using quantum chemical,[19–21] structural,[22,23] spectroscopic,[20,24] and mass spectrometric[25,26] techniques. Crystal structures show that both clusters are oblate, though $Au_9(PPh_3)_8^{3+}$ can take on two different interchanging structural isomers in crystal structures in the presence of different counterions.[23,27] Both clusters are best described within the superatomic model as 6-electron superatoms, having filled $1S$, $1P_x$ (HOMO-1), and $1P_y$ (HOMO) orbitals.[19,20] Despite not featuring a full 8-electron superatomic shell,

their oblate structures are consistent with a geometric stabilization of the $1P_x$ and $1P_y$ and destabilization of the $1P_z$ orbitals such that they feature a large HOMO-LUMO gap. The destabilization of the $1P_z$ orbital is so significant that the apparent LUMO is actually the $1D_{x^2-y^2}$ superatomic orbital rather than $1P_z$ as would be expected.

We previously showed that the optical HOMO-LUMO gap of $Au_8(PPh_3)_7^{2+}$ and $Au_9(PPh_3)_8^{3+}$ could be systematically shifted by varying the substituent in *para-* position of the PPh_3 ligands, and that the magnitude of this shift was strongly correlated to the electron donating strength of substituent as measured by the Hammett *para-* parameter σ_p.[28] Furthermore, the shift was apparently magnified by the higher charge of $Au_9(PPh_3)_8^{3+}$, which we hypothesized to indicate its higher electron withdrawing potential. Subsequent quantum chemical studies broadly reproduced the directions of these trends, but suggested a complex picture.[21]

These studies provided no insight into the underlying chemical principles mediating this control, however. The Hammett equation describes a linear free energy relationship that is defined in the context of the acidity of the carboxylic acid group of benzoic acid,[14] but it has been observed to correlate to a number of commonly encountered chemical observables. The Hammett parameter is interpreted as a measure of electron withdrawing strength (for positive values) and is defined for both *para-* (σ_p) and *meta-* (σ_m) positions relative to the carboxylic acid group. The electron withdrawing or donating effect can be decomposed into inductive (σ_i) and resonance (σ_r) contributions, such that $\sigma_p \approx \sigma_i + \sigma_r$ and $\sigma_m \approx \sigma_i$, where *meta-* substituents lack a resonance component since no probable resonance structure exists for this configuration. Thus, comparing *para-* and *meta-* substituted species makes it possible to determine whether inductive or resonance effects are responsible for an observed linear trend. These parameters are tabulated in Table S2.

Experimental Section

The clusters studied here were synthesized using an approach that has been previously reported,[28] with specific details described in the Supporting Information.

We recorded the electronic absorption spectra of these clusters using a mass spectrometry-based technique that alleviates the need for purification of the as-synthesized reaction mixture—the mass spectrometer is effectively the separation device. The combination of exact selectivity, minimal environmental effects, and low temperature of this experiment yields highly reproducible, well resolved spectra of unambiguously-purified nanoclusters. All experiments were conducted on a home-built ion trap time-of-flight (TOF) mass spectrometer. The experimental process has been explained in detail previously.[29] Briefly, the clusters are introduced into the instrument using electrospray ionization (ESI) of solutions of $\sim$ 1 mg/mL in methanol. Upon storage in a cryogenically-cooled octopole ion trap containing helium, the ions are collisionally cooled to near the trap temperature (3.6-3.8 K), at which point tens of He atoms (referred to as "tags") adsorb onto the clusters. A pulsed optical parametric oscillator, spanning the region 409-719 nm, is intersects the tagged clusters in the cryogenic trap, 10 μs prior to their extraction. Absorption of a photon resonant with the cluster's electronic transitions results in desorption of the all tags, yielding an untagged peak in the mass spectrum. The integrated intensities of the tagged and untagged clusters are recorded as a function of wavelength, and a linear absorption spectrum is generated from the ratio of the latter to the total cluster signal after correcting for the laser power spectrum.

Cluster structures were generated via geometry optimization of reported crystal structures at the BP86+D3[30–32]/cc-pVDZ-pp[33,34] level. Time-dependent density functional theory calculations were performed using the CAM-B3LYP+D3[32,35]/cc-pVDZ-pp functional to avoid well-known charge delocalization errors. Hirschfeld and Mulliken population analyses were performed using the MultiWFN package.[36] All calculations were performed in the ORCA software package.[37]

Results and Discussion

Figure 1 presents the low-energy region of the spectra of all *meta*- substituted clusters studied here. Spectra over a wider range are shown in the Supplementary Information. In the case of $Au_8(PPh_3)_7^{2+}$, $Au_8(P(m\text{-}CH_3\text{-}Ph)_3)_7^{2+}$, and $Au_8(P(m\text{-}OCH_3\text{-}Ph)_3)_7^{2+}$, the HOMO-LUMO transition is easily identified for all three clusters at roughly 2.1 eV. The spectra are decomposed by fitting to a series of Gaussian functions to quantify the transition energies, yielding the dashed curves in Figure 1. For $Au_9(PPh_3)_8^{3+}$, $Au_9(P(m\text{-}CH_3\text{-}Ph)_3)_8^{3+}$, and $Au_9(P(m\text{-}OCH_3\text{-}Ph)_3)_8^{3+}$, identification of the HOMO-LUMO transition is more challenging as it is significantly weaker, likely due to the high symmetry of the cluster. $Au_9(PPh_3)_8^{3+}$ and $Au_9(P(m\text{-}CH_3\text{-}Ph)_3)_8^{3+}$ both feature a single weak transition between 2.0 and 2.1 eV, while $Au_9(P(m\text{-}OCH_3\text{-}Ph)_3)_8^{3+}$ shows two features below 2.2 eV, one at 2.1 eV and one near 1.9 eV. We hypothesized that the lower energy peak was the result of a second isomer, induced by steric hindrance of the bulkier *meta*-$P(Ph{-}OMe)_3$ ligands. This isomerization has been shown to happen, for example in *para*-$P(Ph{-}OMe)_3$-protected Au_9 clusters.[23] We confirmed this hypothesis using two-laser double resonance experiments, as outlined in the Supplemental Information, and thus disregard the 1.9 eV peak for this analysis. We note that, even if the true HOMO-LUMO transition energy were the 1.9 eV peak, the data would still significantly deviate from the trend for *para*- substituted clusters, and thus the conclusions of this work would be unaffected.

Figure 2 plots the HOMO-LUMO transition energies of all *para*- and *meta*- substituted clusters against the corresponding Hammett parameters. It is immediately clear that the strong correlation found for *para*- substituted clusters is not reproduced for *meta*- substituted clusters. Indeed, the transition energies of the *meta*- substituted clusters do not vary monotonically with respect to σ_m, and what variance they do display is substantially smaller than that of the *para*- substituted clusters. Also shown on Figure 2 are linear fits to these trends. As is the case with the *para*- substituted clusters, the *meta*- substituted $Au_8(PPh_3)_7^{2+}$ clusters show a smaller variation than the $Au_9(PPh_3)_8^{3+}$ clusters do, reinforcing the role of

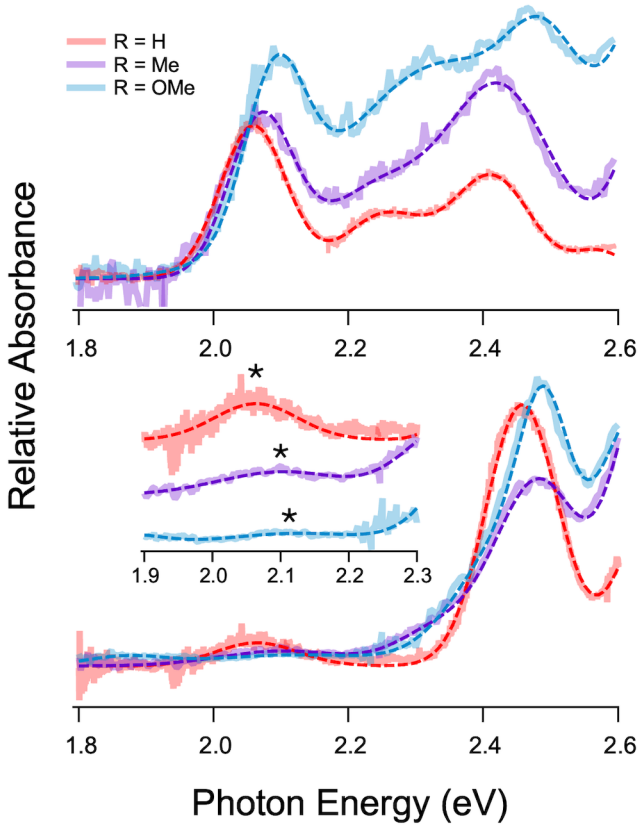

Figure 1: An overview of the spectra of the *meta-* substituted clusters (solid), with corresponding fits to Gaussian absorption features (dashed). Top: the derivatives of $Au_8(PPh_3)_7^{2+}$. Bottom: the derivatives of $Au_9(PPh_3)_8^{3+}$. Inset: a detailed view of the weak apparent HOMO-LUMO transitions (* denotes the absorption max).

the charge of the cluster core in amplifying the ligand effect.

While these results are the typical sign that resonance effects are responsible for the observed control of the HOMO-LUMO energy, the degree to which resonance effect reach into the cluster core remains an open question. We consider two scenarios: a) that resonance extends from the ligand substituent all the way into the cluster core-local superatomic orbitals, or b) that resonance modulates the charge on the phosphorous binding group, which then inductively perturbs the superatomic orbitals. In the former case, we would expect to see a monotonic, or potentially linear, change in bond lengths with respect to σ_p, with alternating shortened and lengthened bonds all the way to the core. In the latter case, we would expect to see a monotonic, or potentially linear, change in the charges of the phosphorous and gold

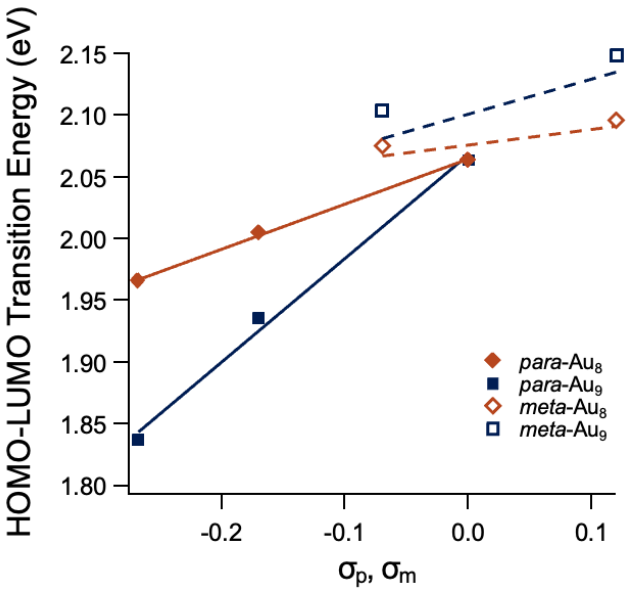

Figure 2: A plot of the HOMO-LUMO transition energies of *para-* (filled markers) or *meta-* (open markers) substituted clusters vs. Hammett σ_p or σ_m, respectively, for $Au_8(PPh_3)_7^{2+}$ and $Au_9(PPh_3)_8^{3+}$ derivatives. Solid lines are linear fits for *para-* substituted clusters, and dashed lines are linear fits for *meta-* substituted clusters.

atoms with σ_p.

Given that the charges and bond lengths are not directly observable in our experiments, we turned to quantum chemical methods to gain further insight. We focus on $Au_8(PPh_3)_7^{2+}$ because there is no uncertainty as to the isomeric structure of this cluster. To determine whether the resonance effects extend into the gold core, we analyzed the computed bond lengths and atomic charges. Resonance electron donating effects at the *para-* position will tend to increase the quinoidal character of the PPh_3 ligand, leading to a shortening of the C_{meta}—C_{ortho} and P—C bond lengths and elongation of the other two aromatic C—C bonds, as shown in the scheme on the top left of Figure 3. If resonance extends to the cluster core, then we expect a lengthening of the Au—P bond with decreasing σ_p. On the left side of Figure 3 is a summary of the computed bond lengths of $Au_8(PPh_3)_7^{2+}$ with each *para-* substituent. We do indeed find the expected alternating pattern of shorter and longer bonds that increases in magnitude with decreasing σ_p of the *para* substituent. Notably, the increase in the Au—P bond length is approximately the same as the increase of the C_{para}—C_{meta}

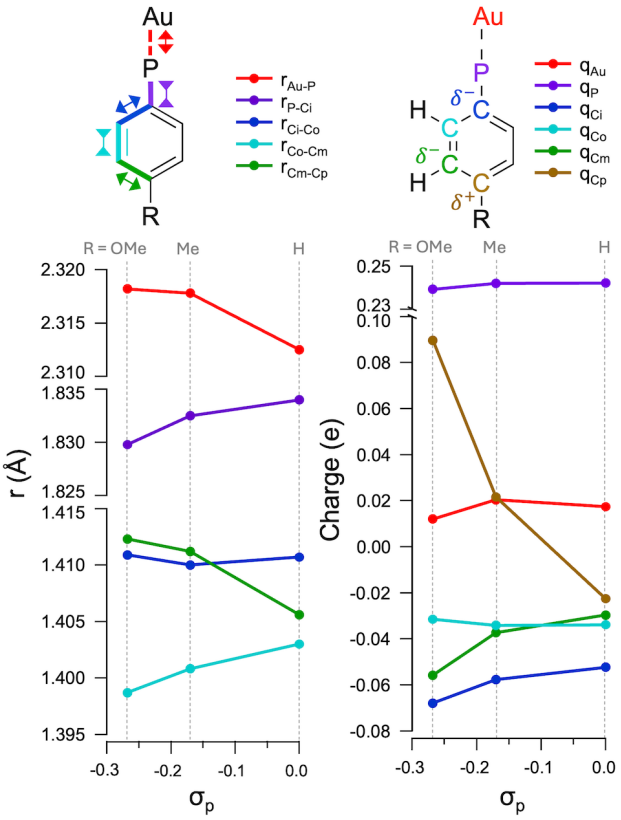

Figure 3: The average bond lengths (left) and atomic charges (right) as computed by BP86+D3/cc-pVDZ-pp for the *para*- substituted $Au_8(PPh_3)_7^{2+}$ clusters with respect to the Hammett *para*- parameter (σ_p). In both cases, quantities are averaged over all chemically equivalent bonds/atoms in the $Au_8(PPh_3)_7^{2+}$ system. At the top is an explanation of the color coding of the figures along with the expected trends as the *para*- substituent changes from H to Me to OMe, assuming resonance is the dominant effect. C_i is the *ipso* carbon with respect to the P atom, C_o is the *ortho* carbon, C_m is the *meta* carbon, and C_p is the *para* carbon.

bond, indicating that the resonance effect has not decayed despite relaying through five bonds. A version of these plots with respect to σ_r is given in Figure S1.

The trends in computed atomic charges are also more consistent with a resonance effect than an inductive effect. Assuming a resonance effect, we expect to see specific trends with decreasing σ_p: increasing charge at the *para-* carbon and decreasing charge at the *meta-* and *ipso-* carbons. In the case of an inductive effect, we would expect the sign of the charge changes to be the same, and to decay for each atom further away from the *para-* carbon. Indeed, we observe the former trend in the computed atomic charges, shown on the right side of Figure 3. We also see a small and monotonic decrease of the charge on the P atom with decreasing σ_p, but we do not see a monotonic change of the charge on the adjacent Au atoms. Since an inductive effect on the Au atom should be most directly driven by the adjacent P atom charge, we conclude that inductive effects are not primarily driving the changes in charges in this cluster.

Applying the same analysis to the computed charges for *meta-* substituted $Au_8(PPh_3)_7^{2+}$as depicted in Figure 4, we again see that the charges on the P atoms vary monotonically with inductive electron donation as measured by σ_m, but the charges on the Au atoms do not. Indeed, the bond lengths and charges for the *meta-* substituted clusters generally do not vary monotonically. Thus, the observed trend in the HOMO-LUMO transition energies can not be explained by an inductive effect from the P atoms, regardless of whether or not resonance effects are significant within the ligands.

Based on the trends in bond lengths and charges, we conclude that the best explanation for the control of the HOMO and LUMO energies afforded by ligand substitution in these clusters is resonance effects, and that the traverses the Au-P bonds to include the cluster core. This is perhaps somewhat surprising because, while the HOMO and LUMO of $Au_8(PPh_3)_7^{2+}$ and $Au_9(PPh_3)_8^{3+}$ are superatomic orbitals delocalized across the cluster core, this result suggests that there is still some clear contribution to those orbitals from Au-ligand bonding that should be able to be rationalized in a manner similar to that of a mononu-

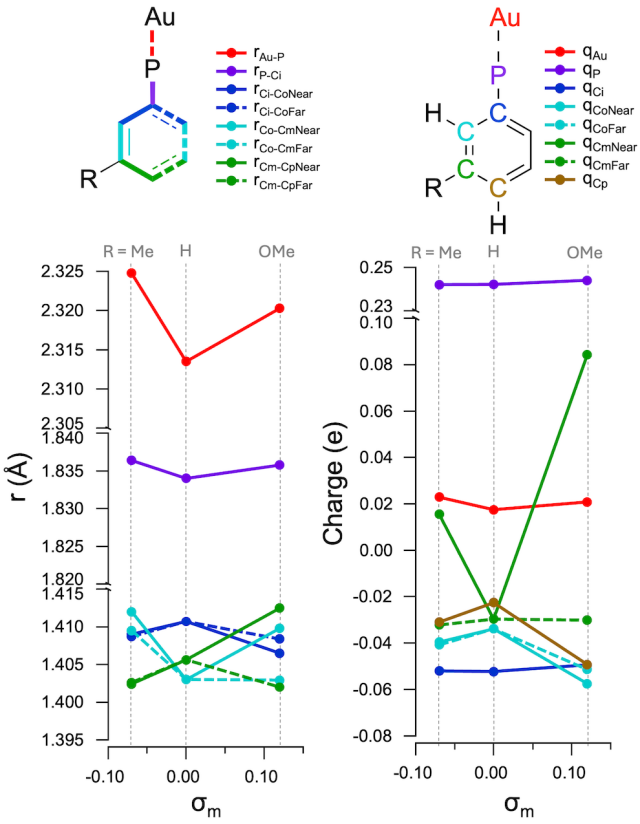

Figure 4: The average bond lengths (left) and atomic charges (right) as computed by BP86+D3/cc-pVDZ-pp for the *meta*- substituted $Au_8(PPh_3)_7^{2+}$ clusters with respect to the Hammett *meta*- parameter (σ_m). In both cases, quantities are averaged over all chemically equivalent bonds/atoms in the $Au_8(PPh_3)_7^{2+}$ system. At the top is an explanation of the color coding of the figures along with the expected trends as the *para*- substituent changes from H to Me to OMe, assuming resonance is the dominant effect. C_i is the *ipso* carbon with respect to the P atom, C_o is the *ortho* carbon, C_m is the *meta* carbon, and C_p is the *para* carbon.

clear coordination complex. We consider two possibilities: that there is a relatively local bonding orbital at the Au-P interface that mixes with the cluster core-based HOMO and/or LUMO superatomic orbitals, or that the HOMO and/or LUMO superatomic orbitals are more extensively delocalized onto the ligands. The fact that the ground state bond lengths and charges show evidence of resonance effects indicates that one of these cases must hold for the HOMO. However, it is unclear if either applies to the LUMO.

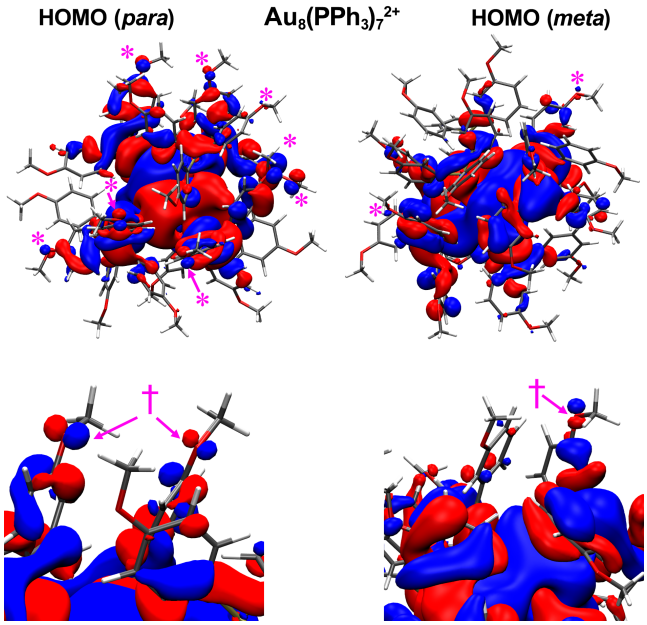

Figure 5: (top) Depictions of the HOMO orbitals for $Au_8(PPh_3)_7^{2+}$ substituted with OMe in the *para*- and *meta*- positions, as determined for an isosurface value of 0.005. Contributions from oxygen atomic orbitals are highlighted by *. (bottom) Images focusing on example oxygen orbital shapes for these orbitals, noted with †, that demonstrate the out of plane nature of the oxygen p orbital in the *para*- case and the in plane nature in the *meta*- case. These orbitals were computed via natural transition orbital analysis.[38]

To determine the degree of delocalization, we performed time-dependent density functional theory calculations of the HOMO-LUMO transition. Indeed, extensive delocalization is observed. Figure 5 presents the HOMO for *para*- and *meta*-OMe-substituted $Au_8(PPh_3)_7^{2+}$, where * highlights OMe oxygen atomic orbital contributions for clarity. Mulliken analysis indicates that the fraction of the hole that sits on these oxygen atoms is ∼7 times greater in the *para*- versus *meta*- case. Further, 38% of the HOMO resides on the ligand in the *para*-

case, compared to only 33% for *meta*-. In contrast, only very modest *para*/*meta* effects are are seen in the LUMO, shown in Figure S2. The large difference in the degree of delocalization in the *para*- versus *meta*- case is again consistent with the assignment of the shift in the HOMO-LUMO transition energy to resonance effects that reach into the Au core. This further indicates that the optical HOMO-LUMO gap shift seen in the experiment is driven by modulation of the hole energy in the excited state. Only some of the OMe groups contribute significantly to the delocalized cluster core orbitals, likely due to a complex interplay of symmetry effects.

Conclusions

Taken together, these results suggest that the intuitive framework developed to rationalize the electronic structures of molecules and complexes likely still holds for nanoclusters, at least up to this size range. Attempts to extend this detailed framework to nanoclusters requires a merging of the delocalized superatomic model of the cluster core with the atomistic picture of bonding commonly invoked in molecular inorganic complexes. Such a framework will be invaluable to facilitate the deliberate engineering of optimized nanoclusters for various applications. Furthermore, the observation of explicit resonance effects extending from the cluster core superatomic orbitals to substituents on the periphery of the ligand shell suggests that the ligand-environment interface can be an active participant in energy and charge transfer processes between the cluster core and the environment. Engineering the ligand-environment interface is thus likely to be an important step in the optimization of nanocluster properties and performance. The observations that resonance effects manifest in both ground state structure and primarily in the HOMO show that this control extends to both ground state and excited state properties.

Acknowledgement

HMH, JB, WW, and CJJ acknowledge support from the United States Department of Energy under grant number DE-SC0021991 and from the Air Force Office of Scientific Research under grant number FA9550-19-1-0105. SO, AM, and BGL gratefully acknowledge support from the the U.S. Department of Energy, Office of Science, Office of Basic Energy Sciences, under Award No. DE-SC0021643 and from the Institute for Advanced Computational Science.

Supporting Information Available

Synthetic and experimental procedures, discussion of isomer study, tabulated Hammett parameters, plots of bond lengths and charges with respect to σ_r, and additional orbital images.

References

(1) Jin, R. Atomically precise metal nanoclusters: stable sizes and optical properties. *Nanoscale* **2015**, *7*, 1549–1565.

(2) Walter, M.; Akola, J.; Lopez-Acevedo, O.; Jadzinsky, P. D.; Calero, G.; Ackerson, C. J.; Whetten, R. L.; Grönbeck, H.; Häkkinen, H. A unified view of ligand-protected gold clusters as superatom complexes. *P. Natl. Acad. Sci. USA* **2008**, *105*, 9157–9162.

(3) Kwak, K.; Lee, D. Electrochemistry of Atomically Precise Metal Nanoclusters. *Accounts Chem. Res.* **2019**, *52*, 12–22.

(4) Jin, R.; Li, G.; Sharma, S.; Li, Y.; Du, X. Toward Active-Site Tailoring in Heterogeneous Catalysis by Atomically Precise Metal Nanoclusters with Crystallographic Structures. *Chem. Rev.* **2021**, 567–648.

(5) Jadzinsky, P. D.; Calero, G.; Ackerson, C. J.; Bushnell, D. A.; Kornberg, R. D. Structure

of a Thiol Monolayer-Protected Gold Nanoparticle at 1.1 Å Resolution. *Science* **2007**, *318*, 430–433.

(6) Knight, W. D.; Clemenger, K.; de Heer, W. A.; Saunders, W. A.; Chou, M. Y.; Cohen, M. L. Electronic Shell Structure and Abundances of Sodium Clusters. *Phys. Rev. Lett.* **1984**, *52*, 2141–2143.

(7) Reber, A. C.; Khanna, S. N. Superatoms: Electronic and Geometric Effects on Reactivity. *Accounts Chem. Res.* **2017**, *50*, 255–263.

(8) Kang, X.; Li, Y.; Zhu, M.; Jin, R. Atomically precise alloy nanoclusters: syntheses, structures, and properties. *Chem. Soc. Rev.* **2020**, *49*, 6443–6514.

(9) Xu, W. W.; Zeng, X. C.; Gao, Y. The structural isomerism in gold nanoclusters. *Nanoscale* **2018**, *10*, 9476–9483.

(10) Takano, S.; Tsukuda, T. Chemically Modified Gold/Silver Superatoms as Artificial Elements at Nanoscale: Design Principles and Synthesis Challenges. *J. Am. Chem. Soc.* **2021**, *143*, 1683–1698.

(11) Wang, Y.; Bürgi, T. Ligand exchange reactions on thiolate-protected gold nanoclusters. *Nanoscale Adv.* **2021**, *3*, 2710–2727.

(12) Niihori, Y.; Koyama, Y.; Watanabe, S.; Hashimoto, S.; Hossain, S.; Nair, L. V.; Kumar, B.; Kurashige, W.; Negishi, Y. Atomic and Isomeric Separation of Thiolate-Protected Alloy Clusters. *J. Phys. Chem. Lett.* **2018**, *9*, 4930–4934.

(13) Griffith, J. S.; Orgel, L. E. Ligand-field theory. *Q. Rev. Chem. Soc.* **1957**, *11*, 381–393.

(14) Hammett, L. P. The Effect of Structure upon the Reactions of Organic Compounds. Benzene Derivatives. *J. Am. Chem. Soc.* **1937**, *59*, 96–103.

(15) Tolman, C. A. Steric effects of phosphorus ligands in organometallic chemistry and homogeneous catalysis. *Chem. Rev.* **1977**, *77*, 313–348.

(16) Mingos, D. M. P.; Lewis, J.; Green, M. L. H. Some theoretical and structural aspects of gold cluster chemistry. *Philos. T. R. Soc. S.-A* **1982**, *308*, 75–83.

(17) Narouz, M. R. et al. N-heterocyclic carbene-functionalized magic-number gold nanoclusters. *Nature Chem.* **2019**, *11*, 419–425.

(18) Hall, K. P.; Theoblad, B. R. C.; Gilmour, D. I.; Mingos, D. M. P.; Welch, A. J. Synthesis and structural characterization of $[Au_9\{P(p\text{-}C_6H_4OMe)_3\}_8](BF_4)_3$; a cluster with a centred crown of gold atoms. *J. Chem. Soc., Chem. Commun.* **1982**, 528–530.

(19) Karimova, N. V.; Aikens, C. M. Time Dependent Density Functional Theory Study of Magnetic Circular Dichroism Spectra of Gold Clusters $Au_9(PH_3)_8^{3+}$ and $Au_9(PPh_3)_8^{3+}$. *J. Phys. Chem. A* **2016**, *120*, 9625–9635.

(20) Fagan, J. W.; Weerawardene, K. L. D. M.; Cirri, A.; Aikens, C. M.; Johnson, C. J. Toward quantitative electronic structure in small gold nanoclusters. *J. Chem. Phys.* **2021**, *155*, 014301.

(21) Day, P. N.; Pachter, R.; Nguyen, K. A. Calculated linear and nonlinear optical absorption spectra of phosphine-ligated gold clusters. *Phys. Chem. Chem. Phys.* **2022**, *24*, 11234–11248.

(22) van der Velden, J. W. A.; Bour, J. J.; Bosman, W. P.; Noordik, J. H. Synthesis and X-ray crystal structure determination of the cationic gold cluster compound $[Au_8(PPh_3)_7](NO_3)_2$. *J. Chem. Soc., Chem. Commun.* **1981**, 1218–1219.

(23) Briant, C. E.; Hall, K. P.; Mingos, D. M. P. Structural characterisation of two crystalline modifications of $[Au_9P(C_6H_4OMe\text{-}p)_{38}](NO_3)_3$: the first example of skeletal isomerism in metal cluster chemistry. *J. Chem. Soc., Chem. Commun.* **1984**, 290–291.

(24) Madridejos, J. M. L.; Harada, T.; Falcinella, A. J.; Small, T. D.; Golovko, V. B.; Andersson, G. G.; Metha, G. F.; Kee, T. W. Optical Properties of the Atomically

Precise C_4 Core $[Au_9(PPh_3)_8]^{3+}$ Cluster Probed by Transient Absorption Spectroscopy and Time-Dependent Density Functional Theory. *J. Phys. Chem. C* **2021**, *125*, 2033–2044.

(25) Hirata, K.; Chakraborty, P.; Nag, A.; Takano, S.; Koyasu, K.; Pradeep, T.; Tsukuda, T. Interconversions of Structural Isomers of $[PdAu_8(PPh_3)_8]^{2+}$ and $[Au_9(PPh_3)_8]^{3+}$ Revealed by Ion Mobility Mass Spectrometry. *J. Phys. Chem. C* **2018**, *122*, 23123–23128.

(26) Muramatsu, S.; Nakahigashi, Y.; Omoda, T.; Takano, S.; Tsukuda, T.; Inokuchi, Y. Collision-Induced Fission of Oblate Gold Superatom in $[Au_9(PPh_3)_8]^{3+}$: Deformation-Mediated Mechanism. *J. Phys. Chem. Lett.* **2023**, *14*, 5641–5647.

(27) Wen, F.; Englert, U.; Gutrath, B.; Simon, U. Crystal Structure, Electrochemical and Optical Properties of $[Au_9(PPh_3)_8](NO_3)_3$. *Eur. J. Inorg. Chem.* **2008**, *2008*, 106–111.

(28) Cirri, A.; Morales Hernández, H.; Kmiotek, C.; Johnson, C. J. Systematically Tuning the Electronic Structure of Gold Nanoclusters through Ligand Derivatization. *Angew. Chem. Int. Ed.* **2019**, *58*, 13818–13822.

(29) Cirri, A.; Hernández, H. M.; Johnson, C. J. High Precision Electronic Spectroscopy of Ligand-Protected Gold Nanoclusters: Effects of Composition, Environment, and Ligand Chemistry. *J. Phys. Chem. A* **2020**, *124*, 1467–1479.

(30) Becke, A. D. Density-functional Exchange-energy Approximation with Correct Asymptotic Behavior. *Phys. Rev. A* **1988**, *38*, 3098–3100.

(31) Perdew, J. P. Density-functional Approximation for the Correlation Energy of the Inhomogeneous Electron Gas. *Phys. Rev. B* **1986**, *33*, 8822–8824.

(32) Grimme, S.; Ehrlich, S.; Goerigk, L. Effect of the damping function in dispersion corrected density functional theory. *J.Comput. Chem.* **2011**, *32*, 1456–1465.

(33) Wilson, A. K.; Woon, D. E.; Peterson, K. A.; Jr., T. H. D. Gaussian basis sets for use in correlated molecular calculations. IX. The atoms gallium through krypton. *J. Chem. Phys.* **1999**, *110*, 7667–7676.

(34) Metz, B.; Stoll, H.; Dolg, M. Small-core multiconfiguration-Dirac–Hartree–Fock-adjusted pseudopotentials for post-d main group elements: Application to PbH and PbO. *J. Chem. Phys.* **2000**, *113*, 2563–2569.

(35) Yanai, T.; Tew, D. P.; Handy, N. C. A new Hybrid Exchange–correlation Functional Using the Coulomb-attenuating Method (CAM-B3LYP). *Chem. Phys. Lett.* **2004**, *393*, 51–57.

(36) Lu, T.; Chen, F. Multiwfn: A Multifunctional Wavefunction Analyzer. *J. Comput. Chem.* **2012**, *33*, 580–592.

(37) Neese, F.; Wennmohs, F.; Becker, U.; Riplinger, C. The ORCA quantum chemistry program package. *J. Chem. Phys.* **2020**, *152*.

(38) Martin, R. L. Natural transition orbitals. *J. Chem. Phys.* **2003**, *118*, 4775–4777.

TOC Graphic